Plasma Physics and
Controlled Fusion

PURPOSE-LED
PUBLISHING™

PAPER

Observation of Alfvén Eigenmodes driven by off-axis neutral beam injection in the TCV tokamak

To cite this article: B Geiger *et al* 2020 *Plasma Phys. Control. Fusion* **62** 095017

View the article online for updates and enhancements.

You may also like

- Simulation of the eigenmode spectrum below the Toroidicity-induced Alfvén eigenmode gap generated by the coupling of Alfvén and slow-magnetosonic waves in tokamaks
G J Kramer, C Z Cheng, M Podestà et al.
- Analysis of Alfven eigenmodes destabilization by energetic particles in TJ-II using a Landau-closure model
J. Varela, D.A. Spong and L. Garcia
- Results from the Alfvén Eigenmode Active Diagnostic during the 2019-2020 JET deuterium campaign
R A Tinguely, P G Puglia, N Fil et al.

This content was downloaded from IP address 194.81.223.66 on 04/02/2025 at 13:11

IOP Publishing Plasma Physics and Controlled Fusion
Plasma Phys. Control. Fusion **62** (2020) 095017 (10pp) https://doi.org/10.1088/1361-6587/aba19e

Observation of Alfvén Eigenmodes driven by off-axis neutral beam injection in the TCV tokamak

B Geiger[1], A N Karpushov[2], P Lauber[3], S Sharapov[4], M Dreval[5], F Bagnato[2], M Baquero-Ruiz[2], A Dal Molin[6], B P Duval[2], M Garcia-Munoz[7], C Marini[8], M Nocente[6], O Sauter[2], L Stipani[2], D Testa[2], M Vallar[2], the TCV[9] and EUROfusion MST1 Teams[10]

[1] UW Madison, Wisconsin, United States of America
[2] Ecole Polytechnique Fédérale de de Lausanne (EPFL), Swiss Plasma Center (SPC), CH-1015 Lausanne, Switzerland
[3] Max-Planck-Institut für Plasmaphysik, Boltzmannstr. 2, 85748 Garching, Germany
[4] Culham Science Centre, Abingdon OX14 3EB, United Kingdom
[5] Institute of Plasma Physics of the NSC KIPT, 61880 Kharkiv, Ukraine
[6] Universita' di Milano-Bicocca, Piazza della Scienza 3, 20126, Milano, Italy
[7] University of Seville, Spain
[8] Oak Ridge Associated Universities, Tennessee, United States of America
[9] see the author list of S Coda *et al* 2019 Nucl. Fusion 59, 112023 (https://doi.org/10.1088/1741-4326/ab25cb)
[10] see the author list of B Labit *et al* 2019 Nu.cl Fusion 59, 086020 (https://doi.org/10.1088/1741-4326/ab2211)

E-mail: benedikt.geiger@wisc.edu

Received 17 February 2020, revised 25 May 2020
Accepted for publication 1 July 2020
Published 31 July 2020

Abstract

Fast-particle driven Alfvén Eigenmodes have been observed in low-collisionality discharges with off-axis neutral beam injection (NBI), electron cyclotron resonance heating (ECRH) and a reduced toroidal magnetic field. During NBI and ECRH, toroidicity induced Alfvén Eigenmodes (TAEs) appear in frequency bands close to 200 kHz and energetic-particle-induced geodesic acoustic modes (EGAMs) are observed at about 40 and 80 kHz. When turning off ECRH in the experiment, those beam-driven modes disappear which can be explained by a modification of the fast-ion slowing down distribution. In contrast, coherent fluctuations close to the frequency of the beam-driven TAEs are present throughout the experiment. The modes are even observed during ohmic plasma conditions, which clearly demonstrates that they are not caused by fast particles and suggests an alternative drive, such as turbulence. The mode-induced fast-ion transport has been found to be weak and marginal in terms of the fast-ion diagnostic sensitivities. Measurements of the plasma stored energy, neutron rates, neutral particle fluxes and fast-ion D-alpha spectroscopy show good agreement with neoclassical modelling results from TRANSP. This is further supported by a similarly good agreement between measurement and modelling in cases with and without ECRH and therefore with and without the modes. Instead, a significant level of charge exchange losses are predicted and observed which generate a bump-on-tail fast-ion distribution function that can provide the necessary free energy to EGAMs.

Keywords: fast particles, tokamak, Alfvén Eigenmodes, off-axis NBI

(Some figures may appear in colour only in the online journal)

 © Ecole Polytechnique Federale de Lausanne Printed in the UK

1. Introduction

Good fast-ion confinement is essential in fusion devices to ensure efficient alpha-particle heating and to protect the first wall from localized losses [1]. While neoclassical transport is typically negligible and below 0.1 $m^2\,s^{-1}$ [2], transport induced by magneto-hydrodynamic mode (MHD) modes such as Alfvén Eigenmodes (AEs) has been observed under certain conditions to be well above 1 $m^2\,s^{-1}$ [3, 4]. Such strong fast-ion transport significantly impacts the fast-ion confinement and has to be avoided in future fusion devices. This, in turn, requires the development of reliable theoretical models that are validated in various regions of parameter space. At the 'Tokamak à Configuration Variable' (TCV) [5, 6] the fast-ion transport can be investigated in a unique parameter space with very large fast-ion fractions. Thanks to the combination of a powerful 1 MW (25 keV) neutral deuterium (D^0) beam source [7] and a relatively small plasma volume of 1 m^3 (TCV has minor and major radii of 0.25 and 0.88 m, respectively), fast-ion densities can even exceed 50% of the electron density [8]. In addition, TCV is equipped with state-of-the-art fast-ion diagnostic, including fast-ion D-alpha (FIDA) spectroscopy [9], neutral particle analyzers [10] and neutron counters [11] and is therefore well suited to test fast-ion models and codes. This paper presents first experiments on neutral-beam driven AEs at TCV. The experimental setup and a representative plasma discharge are introduced in section 2 and section 3 describes the observation of AEs based on magnetic and soft x-ray fluctuation measurements, as well as modelling results based on the linear gyrokinetic code LIGKA[12]. In section 4, fast-ion measurements are compared with TRANSP/NUBEAM [13] modelling and section 5 provides a short summary and outlook.

2. Experimental setup

The experiments described here were performed with a reduced toroidal magnetic field of $B_t = 1.3$ T (compared to 1.43 T) and a plasma current of $I_p = 120$ kA

with flat-top conditions reached after ~ 100 ms. The plasma was operated in the limiter configuration to maintain L-mode conditions throughout the experiment (toroidal beta values are below 0.5%) and the plasma was shifted upwards by 12 cm to achieve off-axis neutral beam injection: The NBI source injects tangentially in the $z = 0$ plane (see figure 1(a)) and upwards-shifting yields a fast-ion deposition profile that is peaked at a normalized toroidal flux label $\rho_t = 0.46$ (see figure 1(b)).

Time traces of a representative experiment are plotted in figure 2. Starting at 0.7 s, NBI heating is applied during four 120 ms long phases with 0.82 MW of power delivered into the TCV vacuum vessel. The small spikes on top of the neutral beam heating power are due to a diagnostic neutral beam (DNB) [14] used for charge exchange recombination spectroscopy (CXRS). Between 0.5 and 1.24 s, the plasma was additionally heated by two 82.7 GHz gyrotrons (X2) that deposit 0.4 MW of ECRH power on the high-field-side at $\rho_t \sim 0.5$. As

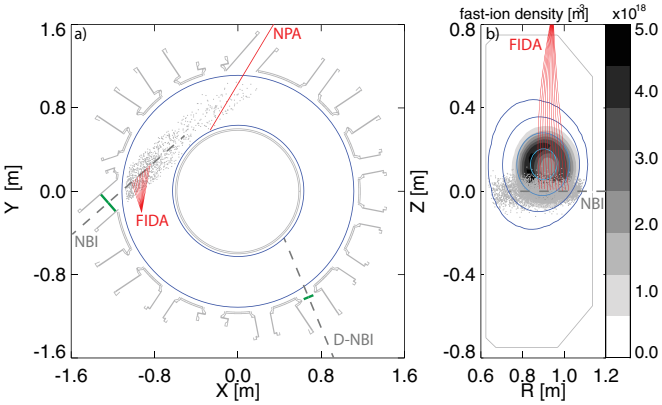

Figure 1. Top-down (a) and poloidal (b) views on the TCV tokamak. Deposition positions of NBI markers from TRANSP are drawn with gray points and the FIDA and NPA viewing geometries are illustrated in red. The gray contours in (b) show the fast-ion density during off-axis NBI and contours of the flux-surfaces are given in blue.

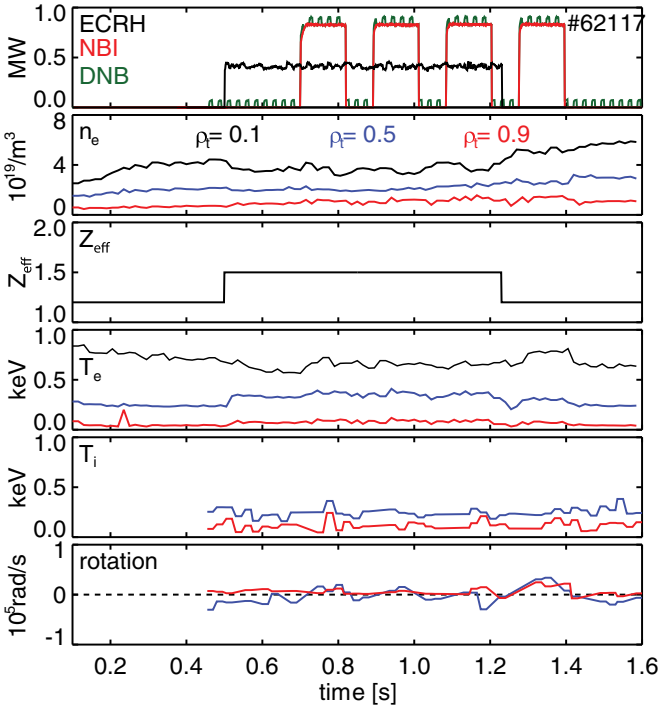

Figure 2. Representative time-traces of discharge #62 117.

displayed in figure 2(b), the core-electron density was close to $4 \times 10^{19}/m^3$ and increased to about $6 \times 10^{19}/m^3$ when ECRH was turned off at 1.24 s. The effective charge (Z_{eff}) profile is considered flat at a value of 1.2 which increases to 1.5 during ECRH. This behaviour has been inferred from comparisons between predicted and measured levels of the loop voltage (see section on TRANSP modelling) and is expected, as ECRH provides an enhanced level of physical sputtering from the carbon walls. The central electron temperature, as plotted in figure 2(d), reaches up to 1 keV and does not increase with the application of off-axis ECRH. In contrast, a clear increase of the electron temperature at $\rho_t \sim 0.5$ can be observed when

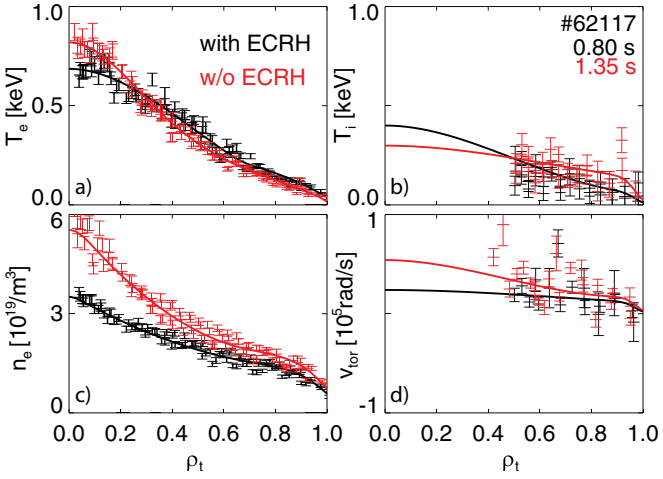

Figure 3. Kinetic profiles of #62 117 at 0.8 and 1.35 s.

ECRH is applied and slightly increased levels become apparent during NBI. Finally, the evolution of the ion temperature and rotation is depicted in figures 2(d)+(f) for $\rho_t = 0.5$ and $\rho_t = 0.9$. Here, it is interesting to note that the application of NBI has only a weak impact on the measured kinetic profiles, suggesting that the absorbed NBI power is low and or that the ion heat and momentum transport are strong.

Figure 3 shows comparisons between measured and fitted (modified hyperbolic tangent function [15]) kinetic profiles for two time-points in discharge #62 117. The experimental electron temperature and density profiles are measured by a vertically aligned Thomson scattering system which covers the whole plasma cross-section, even when shifting the plasma vertically up. In contrast, the impurity ion temperature and rotation is measured by CXRS using the DNB. The latter is located in the $z = 0$ plane and thereby limits the radial coverage of ion-temperature and rotation measurements to $\rho_t > 0.5$. A third order polynomial with a flat profile shape is used to extrapolate the data towards the plasma core. This can be justified since only off-axis external heating sources were applied. However, the lack of central data still provides large uncertainties that need to be considered when analyzing modelling results.

3. Mode activity

The experiments discussed here are rich in MHD activity. This is in part explained by large fast-ion fractions (here, up to 20% of the electron density) and in part by the reduced magnetic field strength ($B = 1.3$ T), which provides Alfvén velocities that are low enough for the excitation of TAEs through 25 keV fast-ions. By considering an ion-density n_i of $1.8 \times 10^{19}\mathrm{m}^{-3}$ (this corresponds to the electron density at $\rho_t = 0.5$, divided by $Z_{\mathrm{eff}} = 1.5$) and $B_t = 1.3$ T, the ratio of the fast-ion velocity, v_{NBI}, to the Alfvén velocity, v_A, reads:

$$\frac{v_{\mathrm{NBI}}}{v_A} = \frac{\sqrt{2E/m_D}}{B/\sqrt{\mu_0 m_D n_i}} \sim \frac{1.55 \times 10^6 \mathrm{ms}^{-1}}{4.72 \times 10^6 \mathrm{ms}^{-1}} \gtrsim \frac{1}{3} \qquad (1)$$

where E is the fast-ion energy (25 keV), m_D is the deuterium mass and μ_0 is the vacuum permeability. The resulting factor of 1/3 is a well-known threshold above which TAEs can be driven by circulating fast-ions through side-band excitation [16].

An overview of the mode activity using three different measurements is given in figure 4. Figure 4(a)+(b) shows radial and poloidal magnetic field fluctuations that are observed by high frequency LTCC-3D magnetic sensors [17] and figure 4(c) shows data from a core-channel of a soft x-ray camera system [18].

3.1. TAEs

Enhanced mode-activity is clearly observed during the first three NBI phases with coherent fluctuations in the 200 kHz range. These beam driven modes have been identified as TAEs with toroidal mode numbers of $n = 2$ and $n = 3$. Figure 5 shows a zoom of the poloidal fluctuation measurement during the third NBI phase, as well as a toroidal mode number analysis based on an array of toroidally distributed magnetic pickup-coils. While the continuous modes, discussed in the next section, are not resolved by the toroidal mode number analysis, beam-driven modes with $n = 2$ and $n = 3$ have clearly been identified. The $n = 2$ modes are chirping between 180 and 130 kHz and the $n = 3$ modes appear in two branches at about 210 and 170 kHz. In addition, theoretical TAE frequencies are plotted in figure 5(b) which have been calculated using [19]:

$$f_{TAE}\,[\mathrm{kHz}] = \left(\frac{v_a}{4\pi qR} + n f_{rot}\right) \cdot 10^{-3} \qquad (2)$$

Here, R is the major radius, f_{rot} the plasma rotation frequency and q is the local safety factor, which is $q = (m + 0.5)/n$ for TAEs [20] with m being the poloidal mode number. To determine the expected TAE frequency for a given q, i.e. combination of (m,n), the radial mode position has been determined using q-profiles from TRANSP (see e.g figure 6(c)). The mode position can then be used to infer corresponding temperature, density and f_{rot} values such that v_A and f_{TAE} can be determined. The resulting frequencies of (5,3), (7,3), (4,2) and (6,2) modes are plotted in figure 4(b) and (agree) very well with the observed frequencies. This observation also agrees well with calculations of the Alfvén continuum [21] that have using the LIGKA code [21], which has been supplied with kinetic profiles and the TRANSP-predicted equilibrium. Figure 6(a)+(b) shows a clear band-gap with reduced continuum damping at the observed frequencies and for the observed poloidal mode numbers. Note here that TAEs appear close to the crossing of two poloidal mode numbers of the Alfvén continuum [22]. An $m = 6$ TAE is for instance expected where the $m = 6$ and $m = 7$ continuum crosses. This can also be seen from the predicted TAE mode structure using the linear gyrokinetic code LIGKA[12]. As can be seen, all observed modes appear between $\rho_t = 0.2$ and $\rho_t = 0.6$.

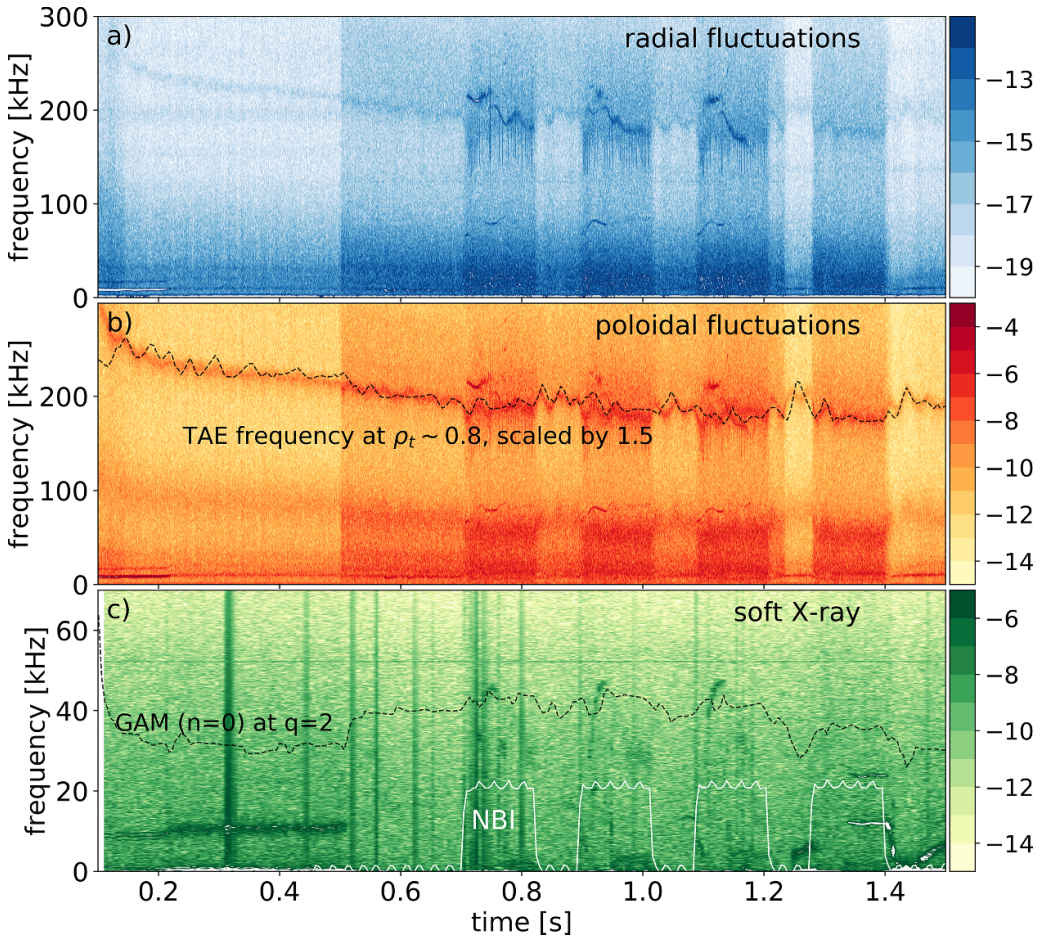

Figure 4. Spectrogram of radial (a) and poloidal (b) fluctuations measured by magnetic pick-up coils. In (b) the scaled ($\times$ 1.5) theoretical frequency of a TAE mode at $\rho_t = 0.8$ ($q \sim 3.7$) is additionally plotted. c) Spectrogram of data from a soft x-ray channel, compared with the expected frequency of a GAM at the $q = 2$ surface.

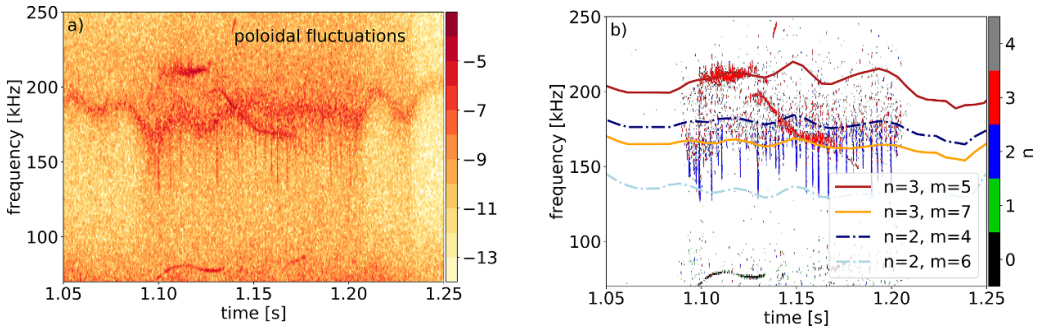

Figure 5. (a) Zoom of the magnetic spectrogram shown in figure 4(b). (b) Toroidal mode number analysis together with the expected frequencies of $n = 3$ and $n = 2$ TAEs with different poloidal mode numbers.

3.2. Continuous modes

In addition to the beam-driven TAEs, coherent fluctuations have been observed at similar frequencies. However, these modes are present throughout the experiment. As can be seen in figure 4, the modes are already present during the ohmic plasma (until 0.5 s), become more intense during pure ECRH and get even stronger when NBI is additionally switched on. The modes clearly follow the evolution of an $n = 0$ TAE at $\rho_t \sim$ 0.8, i.e. at the $q \sim 3.75$ surface (see a dotted line in figure 4(b)) but it was necessary to scale the theoretical TAE frequency by a factor of 1.5 to obtain a good match with the observation. This suggests that the modes are alfvénic but might be of a different kind such as those driven by ellipticity [22]. The hypothesis that the continuous modes are of different origin compared to the beam driven ones is further supported by figure 5(a) where it becomes clear that the modes co-exist with the $n = 2$ and $n = 3$ TAEs. In addition, the continuous modes do not appear in the mode number analysis of figure 5(b) while the TAEs do.

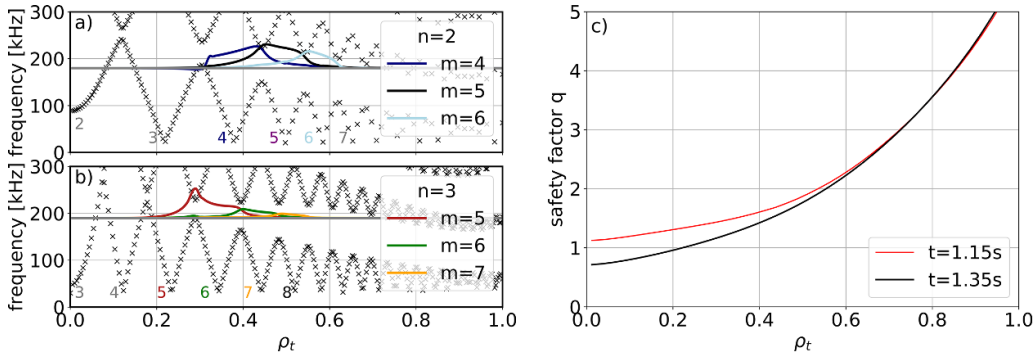

Figure 6. Predicted Alfvén continuum (black crosses) of $n = 2$ (a) and $n = 3$ (b) modes at $t = 1.15$ s. (c) Safety factor profiles for two different time points with and without ECRH.

Such observation of the AEs in the absence of fast particles has previously been reported e.g. at ASDEX Upgrade where the presence of TAEs could be attributed to plasma turbulence [20]. This situation might be similar at TCV where plasmas are typically affected by turbulent fluctuations that develop from unstable trapped electron modes and electron temperature gradient modes [23]. In addition, it should be noted that such an interaction between turbulence and TAEs has recently been observed and studied in non-linear gyrokinetic GENE simulations that suggest a reduction of the turbulence level via coupling to TAEs [24].

Finally it should be noted that observations from the poloidal and radial magnetic sensors are quite different. While the poloidal sensor picks-up the continuous and supposedly turbulence induced modes very well, the radial sensor mainly observes the beam-driven ones. This suggests different polarization directions of the modes and will serve as an important input for comparisons with theoretical and numerical results.

3.3. EGAMs

Upwards chirping modes at about 40 kHz are observed during NBI by the soft x-ray system (called Duplex Multiwire Proportional soft x-ray counter, DMPX). Figure 4(c) shows data from one representative channel where modes can be identified shortly after turning on NBI. The data is compared with the expected frequencies of an $n = 0$ geodesic acoustic mode (GAM), located at the $q = 2$ surface. The GAM frequency has been calculated using [19]:

$$f_{\mathrm{GAM}}[\mathrm{kHz}] = \frac{v_A}{2\pi R}\left[\left(2+\frac{1}{q^2}\right)\beta_s\right]^2 \cdot 10^{-3} \qquad (3)$$

with

$$\beta_s = \frac{c_s^2}{v_A^2} \qquad (4)$$

where c_s is the sound velocity. The good agreement between the predicted and observed frequency and the chirping character of the modes strongly suggests that these are energetic particle driven GAMs (EGAMs) [25, 26].

In addition, EGAMs are expected to be driven by bump-on tail fast-ion distribution functions which are present in TCV due to strong charge-exchange losses (discussed later). Figure 7 displays a TRANSP-predicted fast-ion distribution function for #62 117 as a function of energy, E and pitch $= v_{||}/v_{tot}$ with $v_{||}$ being the velocity parallel to the magnetic field lines and the total velocity v_{tot}. The fast-ion distribution function consists of mainly passing fast ions, peaks at the three injection-energies (25, 12.5 and 8.3 keV) and features positive gradients in E. This provides free energy to excite the $n = 0$ EGAMs that cannot be driven through radial gradients. In addition, figure 7 shows the location of possible wave-particle interactions in black which are given by:

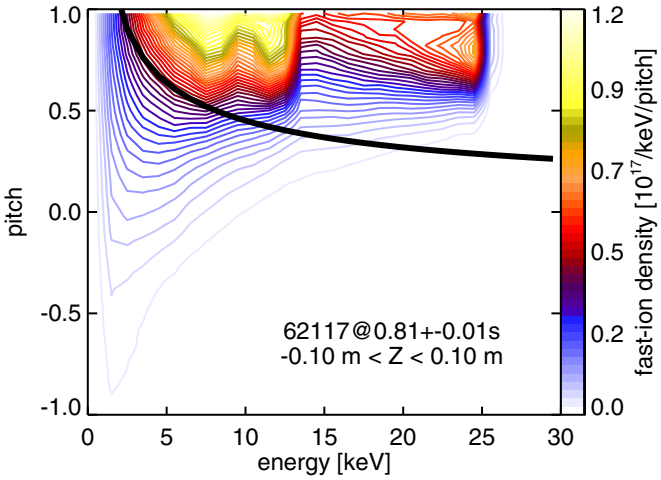

Figure 7. Fast-ion distribution as a function of energy and pitch compared to the pitch-energy resonance line at which 40 kHz EGAMs might be driven.

$$p(E) = \frac{f_{\mathrm{EGAM}} 2\pi R q}{v_{\mathrm{NBI}}(E)} \qquad (5)$$

By employing the observed frequency f_{EGAM} =40 kHz, a resonance line ($p(E)$) is obtained that clearly overlaps with the fast-ion distribution function for $E < 15$ keV where strong velocity space gradients are present. Finally it should be noted that the $n = 0$ character of EGAMs cannot be addressed by the magnetic sensors since these appear to be insensitive to the fluctuations. This might be in part explained by broadband-noise in the magnetic data below 50 kHz and in part by rather

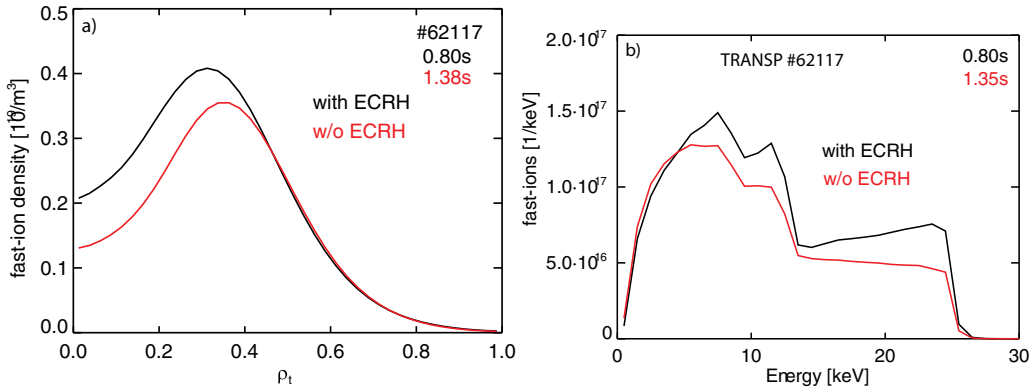

Figure 8. TRANSP predicted radial fast-ion density profile with (black) and without (red) ECRH. (b) TRANSP predicted energy distribution with (black) and without (red) ECRH.

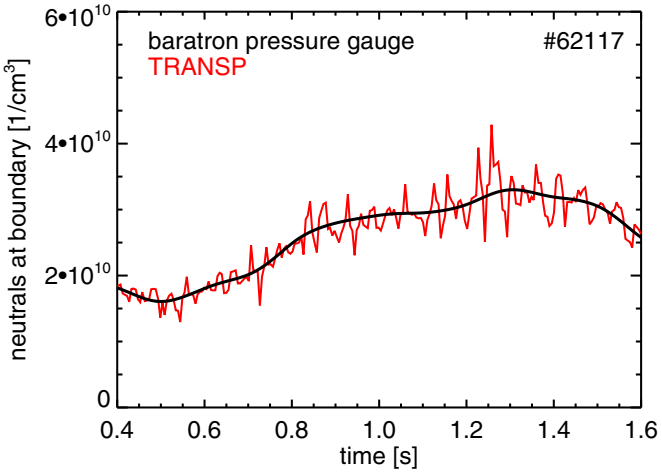

Figure 9. Comparison between the predicted edge neutral density from TRANSP/FRANTIC and the one inferred from a pressure gauge (baratron).

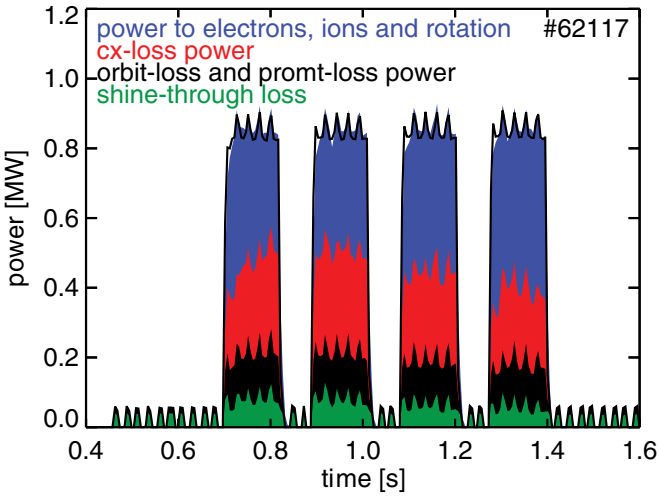

Figure 10. TRANSP-predicted distribution of the injected NBI power into heating and rotation input (blue), charge-exchange losses (red), orbit losses (black) and shine-through (green).

localized radial Eigenfunctions of those modes. In contrast, there are $n = 0$ modes observed in the LTCC-3D data at about 80 kHz (see figure 5(b)). For these modes, however, it is not clear whether they are EGAMs, as the expected frequencies (equation (3)) would only match for core-localized modes (near $q = 1$) where strong damping is expected. Unfortunately, the modes are not seen in data from the soft x-ray system due to bandwidth-problems which restricts our analysis to about 70 kHz.

3.4. Absence of beam-driven Alfvén modes without ECRH

During the 4th NBI phase in discharge #62 117 (1.28–1.4 s), ECRH was turned off. Interestingly this phase does not exhibit NBI-driven fluctuations, which might be explained by either increased damping (stability) or by a reduced drive of the modes. In particular for the TAEs, the damping seems not to be affected significantly since the coherent fluctuations from the possibly turbulence-driven modes are still present (see figure 4(a)). In addition, the q-profile is not strongly modified at $\rho_t \sim 0.5$ where the beam driven modes have been localized (see figure 6(b)).

In contrast, the slowing down time is reduced when switching off ECRH as the electron temperature decreases and the electron density peaking increases. This reduces the off-axis fast-ion density and the bump-on tail character. Figure 8 compares TRANSP-predicted fast-ion distribution functions as a function of ρ_t and energy for the cases with and without ECRH. The predicted fast-ion density is clearly lower without ECRH and features a reduced gradient at E. A similar effect has e.g. been reported by [27] where ICRF-driven TAEs were observed only when applying additional ECRH, which enhanced the slowing down time.

4. TRANSP modelling

The fast-ion densities shown above have been calculated using the TRANSP code. The code has been supplied with the fitted kinetic profiles and Z_{eff} values as already shown in figures 2 and 3. In addition, information on the NBI and ECRH systems,

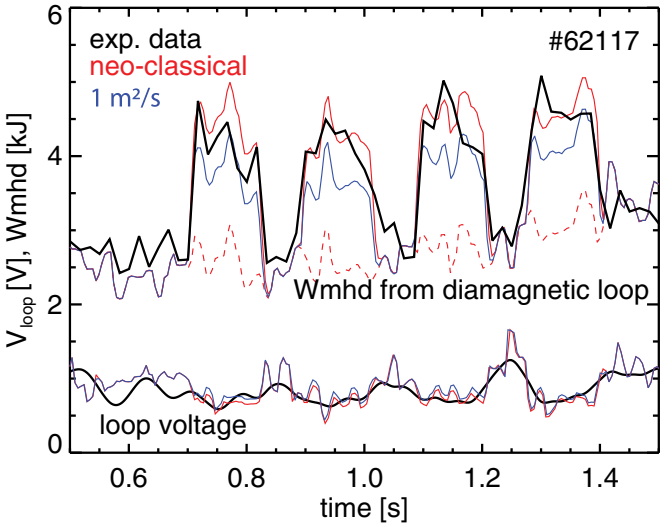

Figure 11. Measured loop voltage (around 1 eV) and plasma stored energy (about 5 kJ) compared with predictions from TRANSP. The simulation in red corresponds to the assumption of neoclassical fast-ion transport while the simulation in blue refers to a global anomalous transport of 1 m^2 s^{-1}. The dashed red line shows the simulated evolution of the plasma stored energy without considering fast particles.

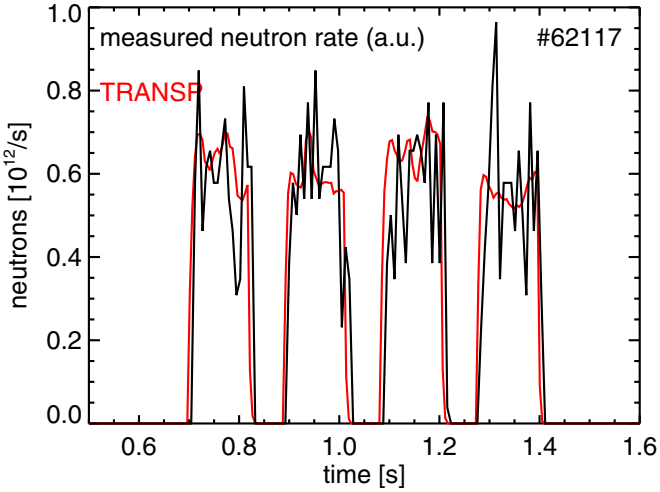

Figure 12. Measured neutron rates compared to a neoclassical TRANSP simulation (red).

the evolution of the plasma boundary, the central magnetic field strength, the plasma current and the background neutral density have been provided.

Careful treatment of the neutral density is important for TRANSP simulations of TCV plasmas since charge exchange losses alter the fast-ion density significantly [8]. Here, the FRANTIC module of TRANSP has been used to determine the shape of a 1D neutral density profile used in TRANSP. The absolute level of this profile is set by defining a global particle confinement (see also [8]), which has been chosen such that the resulting edge-neutral density matches experimental data deduced from a baratron pressure gauge (see figure 9).

The predicted edge-neutral density is about $3 \times 10^{16}/m^3$ and causes, in combination with the off-axis NBI population, strong charge-exchange losses. Figure 10 illustrates the distribution of the injected NBI power into plasma heating and momentum input (blue), as well as losses which sum up to about 50% of the input power. The losses consist of charge exchange losses (red), orbit losses (black) and shine-through (green). The contribution of charge exchange is particularly strong for off-axis injection in TCV since the small minor radius of TCV allows the neutral density to reach half radius without strong attenuation (only about a factor of 10). Under these conditions, the characteristic time for charge exchange is smaller than the slowing-down time such that the beam distribution function does not relax to the slowing-down form. In consequence a fast-ion energy distribution with positive gradients is obtained (see figures 7 and 8(b)).

Figure 11 shows a comparison of TRANSP predictions with measurements of the loop voltage and of the plasma stored energy (3/2 of the perpendicular energy as measured by a diamagnetic loop). As can be seen, modelling and experiment are in good agreement which shows that the kinetic profiles and the corresponding calculation of the fast-ion pressure and current drive are consistent. During each NBI phase, the plasma stored energy increases. This increase is due to the additional presence of fast particles while the stored energy from the thermal plasma (dashed line) is expected to remain constant. Here, it should be noted that the uncertainties of the central ion-temperature are large. However, the plasma stored energy is weighted towards the outer radii since the core part contributes only with a small fraction of the plasma volume. Concerning the loop voltage, we adjusted the Z_{eff} value in TRANSP to match the level of the loop voltage. Thus, it is no surprise that we obtain an overall good agreement between measurement and modelling. However, the simulation even follows the NBI-induced variations of the loop voltage, which suggest that the fast-ion current drive is modelled consistently. In addition to the neo-classical simulation in red, figure 11 shows (in blue) results from a simulation considering an ad-hoc fast-ion diffusion of 1 m^2 s^{-1}. While the assumption of additional anomalous transport hardly changes the predicted loop-voltage, the predicted plasma stored energy is lower and slightly under-estimates the measurement.

In addition, the evolution of the fast ion density from TRANSP can be validated by the comparison with neutron rates, radial FIDA intensity profiles and NPA measurements. Experimental neutron rates are plotted in figure 12. The experimental data is not absolutely calibrated and has been scaled to the neoclassical TRANSP simulation (red) by one factor such that only the evolution of the simulation and measurement can be evaluated. As can be seen, measurement and simulation agree well during all four phases which allows us to conclude that a possible anomalous transport induced by the beam-driven modes (not considered by TRANSP) is below the measurement sensitivity. If there was a significant loss of fast-ion confinement during the first three NBI phases, we would see enhanced neutron rates during the fourth phase when the modes are gone (without ECRH).

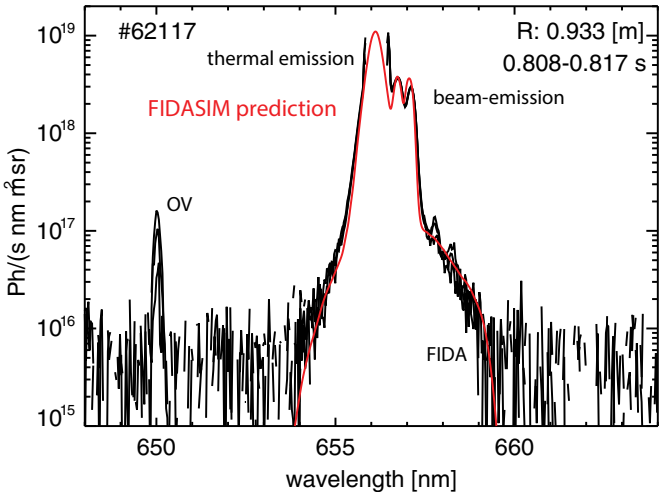

Figure 13. Exemplary FIDA spectrum of #62 117 compared with a synthetic spectrum from FIDASIM (red) which corresponds to the neoclassical TRANSP simulation.

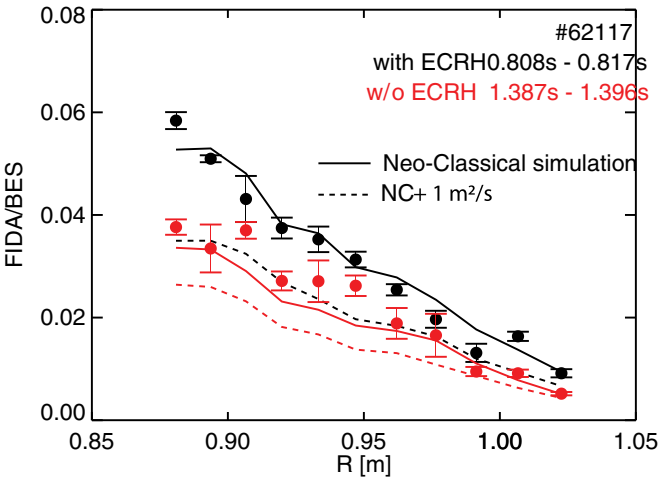

Figure 15. Radial FIDA intensity profiles with (black) and without ECRH (red). Corresponding neo-classical TRANSP/FIDASIM simulations are plotted with solid lines while simulations assuming anomalous transport are shown with dashed lines.

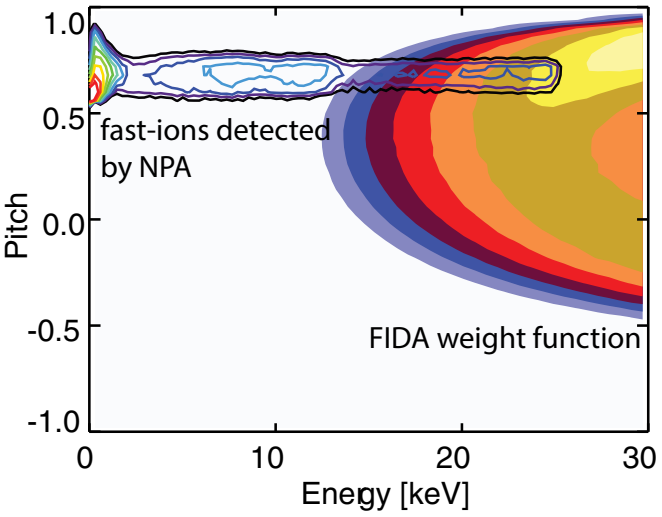

Figure 14. FIDA weight function (filled contour plot) and energy-pitch distribution of fast-ions being detected by the CNPA diagnostic (solid contours).

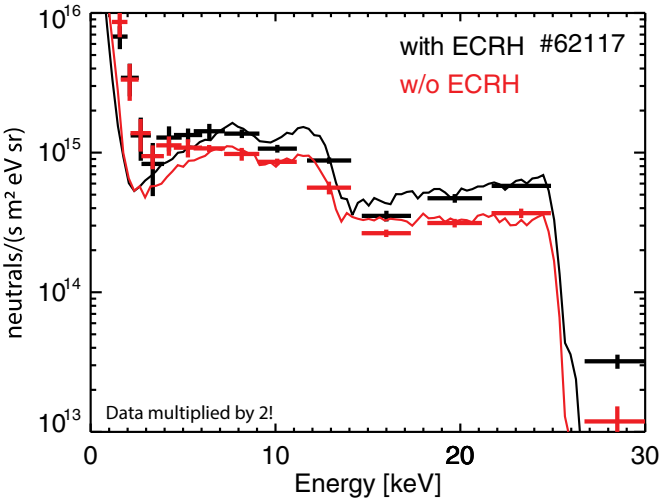

Figure 16. Energy spectra from the NPA detector compared with FIDASIM modelling results. The experimental data has been scaled by a factor of two for both cases, i.e. for the data with ECRH (black) and without ECRH (red).

A similar observation is made when analyzing data from FIDA spectroscopy. The FIDA system at TCV uses an array of lines of sight that intersect the neutral beam from top-down at different radial positions (see figure 1). Four representative spectra of a central channel are plotted in figure 13. Passive radiation, measured after turning off NBI, has been subtracted such that the spectra mainly consist of active contribution: the beam-emission, the thermal charge-exchange emission (halo) and the contribution from neutralized fast ions (FIDA light). Due to the NBI and observation geometries, mainly red-shifted FIDA radiation can be analyzed. The part of velocity space covered by studying FIDA radiation between 658.5 and 659.5 nm is depicted in figure 14 using a weight function [28]. The weight-function shows that the diagnostic provides information on fast ions with energies above 12 keV and dominantly positive pitch values.

Radial FIDA profiles are obtained by integrating the FIDA emission of each line of sight in the specified wavelength interval (658.5–659.5 nm). By further dividing the FIDA emissivity by the observed level of the beam emission, FIDA/BES profiles are obtained which are independent of an intensity calibration and permit comparison with modelling results from FIDASIM [29]. FIDASIM uses TRANSP predicted fast-ion distribution functions as input and provides synthetic spectra of the beam, halo and FIDA emission that can be integrated to obtain synthetic profiles. Figure 15 shows a comparison of predicted and measured radial FIDA/BES profiles for a time-point with ECRH ($\sim$ 0.8 s) and a time-point without ECRH ($\sim$ 1.38 s). As can be seen, the measurements and neo-classical simulations (solid lines) agree very well. In addition, the FIDA/BES profile is higher during the phase with

ECRH (red) which is expected due to modified kinetic profiles. The dashed lines in figure 15 represent synthetic profiles resulting from the TRANSP simulation assuming additional anomalous fast-ion transport of 1 $m^2\ s^{-1}$. These profiles clearly under-estimate the measurement and demonstrate that possible anomalous transport is well below this level.

In addition, FIDASIM has been used to obtain synthetic neutral particle analyzer (NPA) measurements that can be compared with the measurements of the compact NPA system of TCV. The viewing geometry of the NPA is illustrated in figure 1 and the part of velocity space accessed by the NPA is depicted in figure 14. Energy spectra measured by the NPA detector for time points with and without ECRH are shown in figure 16. During ECRH, the fast-ion part of the signal ($E > 2$ keV) is higher and slightly more peaked towards the injection energy than what is measured without ECRH. This behaviour is reproduced by FIDASIM, suggesting that the predicted fast-ion distribution function from TRANSP is valid. However, it should be noted that the data has been scaled by a factor of two in order to match the simulation. This factor might be explained by a degradation of the NPA detector or by a neutral density that is much smaller along the NPA view than what is expected by TRANSP/FRANTIC. Nevertheless, the shape and trend measured by the NPA diagnostic are well reproduced by the modelling. During ECRH, the measurement is considerably higher and features a stronger gradient towards higher energies than what is seen without ECRH. This again supports the conclusion that the mode-induced fast-ion transport is relatively weak.

5. Summary and outlook

The fast-ion confinement has been investigated in off-axis NBI experiments at TCV with a reduced magnetic field strength of 1.3 T. For the first time, clear NBI-induced AE activity has been observed which consists of TAEs and EGAMs. While the EGAMs are driven by a bump-on tail fast-ion distribution function present due to strong charge exchange losses, the TAEs occur in a gap-structure around mid-radius with toroidal mode numbers of $n = 2$ and $n = 3$. The NBI-driven modes are only present when off-axis ECRH is on, as demonstrated by one NBI phase without additional electron heating. This observation is likely explained by reduced fast-ion densities due to shorter slowing down times. The fast-ion measurements agree very well with this hypothesis and demonstrate that the fast-ion confinement is close to its neoclassical level. Moreover, the observed modes do not alter the fast-ion confinement to a noticeable level as no confinement-improvement is seen during the phase without TAEs and EGAMs. This experimental demonstration could already be a test case for codes that predict anomalous fast-ion transport and shows that, in the presence of only few modes, the fast-ion transport remains weak. In addition, continuous AE activity at about 200 kHz has been observed with modes present even during ohmic plasma conditions. This suggests that the modes are not driven by fast particles and other mechanisms such as turbulence need to be considered. The observation of this continuous AE type might therefore allow future experimental studies, analyzing the interplay between turbulence and Alfvén modes.

Acknowledgments

We would like to thank Prof. William Heidbrink for his help in interpreting the observed mode activity during his stay in Lausanne.

This work has been carried out within the framework of the EUROfusion Consortium and has received funding from the Euratom research and training programme 2014–2018 and 2019–2020 under Grant Agreement No 633053. The views and opinions expressed herein do not necessarily reflect those of the European Commission. Moreover, this work was supported in part by the Swiss National Science Foundation.

ORCID iDs

B Geiger https://orcid.org/0000-0001-8706-1874
S Sharapov https://orcid.org/0000-0001-7006-4876
C Marini https://orcid.org/0000-0003-4819-7765
M Nocente https://orcid.org/0000-0003-0170-5275
L Stipani https://orcid.org/0000-0002-7797-5864
M Vallar https://orcid.org/0000-0002-1792-6702

References

[1] Fasoli A *et al* 2007 Chapter 5: Physics of energetic ions *Nucl. Fusion* **47** S264–S284
[2] Heidbrink W and Sadler G 1994 The behaviour of fast ions in tokamak experiments *Nucl. Fusion* **34** 535–615
[3] Turnyanskiy M *et al* 2013 Measurement and control of the fast ion redistribution on MAST *Nucl. Fusion* **53** 053016
[4] Collins C S *et al* 2016 Observation of critical-gradient behavior in alfvén-eigenmode-induced fast-ion transport *Phys. Rev. Lett.* **116** 095001
[5] Fasoli A 2009 Overview of physics research on the TCV tokamak *Nucl. Fusion* **49** 104005
[6] Fasoli A 2015 TCV heating and in-vessel upgrades for addressing DEMO physics issues *Nucl. Fusion* **55** 043006
[7] Karpushov A N *et al* 2015 Upgrade of the tcv tokamak, first phase: Neutral beam heating system *Fusion Eng. Des.* **96–97** 493–7 *Proc. of the 28th Symp. On Fusion Technology (SOFT-28)*
[8] Geiger B *et al* 2017 and and, 'Fast-ion transport in low density l-mode plasmas at TCV using FIDA spectroscopy and the TRANSP code' *Plasma Phys. Control. Fusion* **59** 115002
[9] Heidbrink W W, Burrell K H, Luo Y, Pablant N A and Ruskov E 2004 Hydrogenic fast-ion diagnostic using Balmer-alpha light *Plasma Phys. Control. Fusion* **46** 1855–75
[10] Karpushov A N, Duval B P, Schlatter C, Afanasyev V I and Chernyshev F V 2006 Neutral particle analyzer diagnostics on the tcv tokamak *Rev. Sci. Instrum.* **77** 033504
[11] Xufei X *et al* 2014 Neutron measurements from beam-target reactions at the elise neutral beam test facility *Rev. Sci. Instrum.* **85** 11D864
[12] Lauber P, Guenter S, Koenies A and Pinches S 2007 Ligka: A linear gyrokinetic code for the description of background kinetic and fast particle effects on the MHD stability in tokamaks *J. Comput. Phys.* **226** 447–65

[13] Pankin A, McCune D, Andre R, Bateman G and Kritz A 2004 The tokamak Monte Carlo fast ion module nubeam in the national transport code collaboration library *Comput. Phys. Commun.* **159** 157–84
[14] Karpushov A N *et al* 2003 Upgrade of the diagnostic neutral beam injector for the TCV tokamak *Fusion Eng. Des.* **66–68** 899–904 *22nd Symp. on Fusion Technology*
[15] Groebner R J and Osborne T H 1998 Scaling studies of the high mode pedestal *Phys. Plasmas* **5** 1800–6
[16] Biglari H, Zonca F and Chen L 1992 On resonant destabilization of toroidal Alfvén Eigenmodes by circulating and trapped energetic ions/alpha particles in tokamaks *Phys. Fluids* B **4** 2385–8
[17] Testa D, Corne A, Farine G, Jacq C, Maeder T and Toussaint M 2015 3d, ltcc-type, high-frequency magnetic sensors for the tcv tokamak *Fusion Eng. Des.* **96–97** 989–92 *Proc. of the 28th Symp. On Fusion Technology (SOFT-28)*
[18] Sushkov A, Andreev V, Camenen Y, Pochelon A, Klimanov I, Scarabosio A and Weisen H 2008 High-resolution multiwire proportional soft x-ray diagnostic measurements on tcv *Rev. Sci. Instrum.* **79** 023506
[19] Fesenyuk O P, Kolesnichenko Y I and Yakovenko Y V 2013 Frequencies of the geodesic acoustic mode and alfvén gap modes in high-q2β plasmas with non-circular cross section *Phys. Plasmas* **20** 122503
[20] Maraschek M, Günter S, Kass T, Scott B, Zohm H and Team A U 1997 Observation of toroidicity-induced Alfvén Eigenmodes in ohmically heated plasmas by drift wave excitation *Phys. Rev. Lett.* **79** 4186–9
[21] Lauber P, Brüdgam M, Curran D, Igochine V, Sassenberg K, Günter S, Maraschek M, Garcia-Munoz M, Hicks N and the ASDEX Upgrade Team 2009 Kinetic Alfvén Eigenmodes at ASDEX Upgrade *Plasma Phys. Control. Fusion* **51** 124009
[22] Heidbrink W W 2008 Basic physics of alfvén instabilities driven by energetic particles in toroidally confined plasmas *Phys. Plasmas* **15** 055501
[23] Merlo G, Fontana M, Coda S, Hatch D, Janhunen S, Porte L and Jenko F 2019 Turbulent transport in tcv plasmas with positive and negative triangularity *Phys. Plasmas* **26** 102302
[24] Siena A D, Görler T, Poli E, Navarro A B, Biancalani A and Jenko F 2019 Electromagnetic turbulence suppression by energetic particle driven modes *Nucl. Fusion* **59** 124001
[25] Fu G Y 2008 Energetic-particle-induced geodesic acoustic mode *Phys. Rev. Lett.* **101** 185002
[26] Horváth L *et al* 2016 Experimental investigation of the radial structure of energetic particle driven modes *Nucl. Fusion* **56** 112003
[27] Sharapov S E *et al* 2017 The effects of electron cyclotron heating and current drive on toroidal Alfvén Eigenmodes in tokamak plasmas *Plasma Phys. Control. Fusion* **60** 014026
[28] Salewski M *et al* 2014 On velocity-space sensitivity of FIDA spectroscopy *Plasma Phys. Control. Fusion* **56** 105005
[29] Heidbrink W W, Liu D, Luo Y, Ruskov E and Geiger B 2011 A code that simulates fast-ion d-alpha and neutral particle measurements *Commun. Computat. Phys.* **10** 716–41